Impact of spherulite-type crystalline defects on the mechanical and electrochemical properties of Ti(40)Cu36Zr(10)Pd(14) metallic glasses

Laurabelle Gautier, Alethea Liens, Benoit Ter-Ovanessian, Sabrina Marcelin, Thierry Douillard, Herve Richard, Nicolas Courtois, Jerome Chevalier, Damien Fabrègue

Version of Record: https://www.sciencedirect.com/science/article/pii/S2589152922000400
Manuscript_68e3a582f323d9f235957aedc0293771

Impact of spherulite-type crystalline defects on the mechanical and electrochemical properties of TiCuZrPd metallic glasses

Authors and affiliation

Laurabelle Gautier[a] <laurabelle.gautier@insa-lyon.fr>

Aléthea Liens[a] <aliens@anapath.ch>

Benoit Ter-Ovanessian[a] <benoit.ter-ovanessian@insa-lyon.fr>

Sabrina Marcelin[a] <sabrina.marcelin@insa-lyon.fr>

Thierry Douillard[a] <thierry.douillard@insa-lyon.fr>

Hervé Richard [b] <herve.richard@anthogyr.com>

Nicolas Courtois[b] <nicolas.courtois@anthogyr.com>

Jérôme Chevalier[a*] **corresponding author** <jerome.chevalier@insa-lyon.fr>

Damien Fabrègue[a] < damien.fabregue@insa-lyon.fr>;

[a] INSA-Lyon, MATEIS Laboratory, University of Lyon, UMR CNRS 5510, 20 Avenue Albert Einstein, 69621 Villeurbanne CEDEX, France;

[b]Anthogyr SAS, 2237 Avenue A. Lasquin, 74700 Sallanches, France;

Abstract

One of the limitations to the use of certain bulk metallic glasses is related to the formation of crystalline zones or defects, often called “spherulites”, during the casting process. In the case of $Ti_{40}Zr_{10}Cu_{36}Pd_{14}$ (at %) metallic glass, which is a candidate for biomedical applications, spherulites of diameter up to few hundreds of microns were previously reported, but their crystallographic features and their role in the mechanical behavior and the corrosion resistance remains to be determined.

In this work, a detailed description of the microstructure of spherulites is provided. Tensile, compression and fatigue tests were carried out. In addition, corrosion behavior was studied by global and local electrochemical measurements. The spherulites have a deleterious effect on the tensile and fatigue strength of the alloy, even if it still retains strength properties that are far superior to conventional crystalline materials. The electrochemical studies do not show any difference in potential between the spherulite and the amorphous matrix, which indicates that the presence of spherulites is probably not the direct cause of the pitting phenomenon observed, which is unfortunately a clear drawback of this alloy when considering biomedical implants.

Keywords

Ti-based bulk metallic glass, crystalline defects, biomaterials, dental implant, mechanical characterisation, corrosion resistance, fatigue properties, microstructural characterization.

1 Introduction

There are only few articles in the literature dealing with spherulite crystalline defects in amorphous metals. This might be in part due to the use of X-Ray Diffraction, generally used to check if cast rods are amorphous or crystalline. In most cases, samples having diffractograms that show broad halo peak without any distinct peaks originating from the crystalline phase are considered as 'amorphous' [1,2]. This macroscopic characterization may not be precise enough to assess the presence of spherulites in small overall content. Another possible origin to the low number of publications concerning spherulites is the difficulty of observing them before and after mechanical testing. In most studies on Bulk Metallic Glasses (BMG), the authors focus on compression test. However, it was shown in [2] that casting defects in the TiCuZrPd grade were not visible on the fracture surface of parts tested in compression, whereas they were clearly visible on samples tested in tension [2,3].

These defects can be large in size, randomly distributed and can therefore negatively affect the mechanical properties of the material [2,4,5], in particular by causing premature failure in tension and/or cyclic fatigue. The presence of spherulites may have a negative effect on fracture toughness, as it was shown in 3 points bending test on pre-cracked samples of an ZrCuAlNi BMG [5,6]. On the other side, some authors consider the presence of a crystalline phase surrounded by an amorphous matrix as an opportunity to improve the mechanical resistance of BMGs. It has been reported in the literature [7–9] mainly on CuZr(Ti or Al) ternary alloys, that the spontaneous formation of a B2 phase during the casting of the rods, if the crystalline particles are controlled in size and homogeneously distributed in the parts, can bring ductility and thus improve the usual completely brittle behavior of this grade.

If few papers are dealing with a deep characterization of spherulites in some BMG and others tend to show that they may have an effect on mechanical properties, there is not so far, a comprehensive characterization in $Ti_{40}Cu_{36}Zr_{10}Pd_{14}$ alloys, while they are often cited as promising candidates for biomedical applications [2,10]. This publication therefore aims at highlighting the presence (by a morphological and chemical characterization) of spherulite-type crystalline defects in the widely studied

$Ti_{40}Zr_{10}Cu_{36}Pd_{14}$ (at %) grade and their influence on the overall material's mechanical properties and corrosion resistance. This paper suggests a quite simple sample preparation protocol for the clear observation of spherulites in optical and SEM microscopy. It will question the use of X-rays for the verification of the amorphous character of the parts. It will also focus on the link between the presence of these spherulites and the mechanical properties obtained. The difference in tension and in compression will be discussed (as well as the different fracture modes involved). In view of an application for dental implants, some prototypes were tested in bending and fatigue following the ISO14801 standard[11] used generally for endo-osseous dental implants, which could be a potential application[2,12–14]. Indeed, the interests of using such material for dental implant application are its high strength, allowing the miniaturization of implants and its Young's modulus, lower than crystalline titanium alloys, which would decrease stress shielding phenomena. Finally, an electrochemical study involving local measurements and detailed observations to determine the influence of spherulites on corrosion resistance will be presented.

2 Materials and Methods

2.1 Material processing

The ingots with a targeted composition of $Ti_{40}Zr_{10}Cu_{36}Pd_{14}$ (at. %) were prepared by arc melting from pure elements (purities above 99.9%). Rods with a diameter of 5 mm were prepared using a tilt copper mold-casting apparatus in a high-purity argon atmosphere. The composition of all the ingots was controlled by Energy-Dispersive X-ray Spectroscopy (EDXS) on a Scanning Electron Microscope (SEM) at an acceleration voltage of 15 keV.

2.2 Sample characterisation

2.2.1 X-Ray diffraction

After the production of the BMG rods, the amorphous state of the samples was checked by X-Ray Diffraction (XRD) with a Bruker AXS D8 (Billerica, Massachusetts, USA) machine equipped with a copper tube. The X-Ray tube was set at 4 KeV voltage and 40mA current with a Cu K_α of 1.54 Å irradiation wavelength. The detector used was a Lynxeye, which was used over a range 2θ from 10 to 70° with an 0.0167° increment,

with a slit of 0.6 mm and a scan speed of 1s/step. The post-acquisition processing of the diffractograms was conducted on the Eva software (Bruker).

2.2.1.1 Optical microscopy

The observations of the spherulites in optical microscopy were conducted after different polishing steps on a Buehler semi-automatic polishing machine Ecomet 250 (Esslingen, Germany), first with SiC papers successively with grains of #600, #800, #1200 and #2500. The final mechano-chemical polishing step was performed on a Buehler ChemoMet synthetic polishing pad with a solution made of 75% of colloidal silica suspension and 25% H_2O_2. The optical microscopy pictures were then taken with a Hirox RH-2000 digital microscope (River Edge, NJ, USA).

2.2.2 Hardness tests

The hardness measurements were performed on a Buehler Micromet 5140 machine (Esslingen, Germany). The samples were first mirror polished and the measurements were conducted with a load of 0.5kgF. They were repeated fifteen times on the spherulites and on the amorphous matrix.

2.2.3 Scanning Electron Microscopy (SEM)

The observation of polished and fracture surfaces was carried out by SEM (Zeiss Supra 55, Oberkochen, Germany), using an acceleration voltage of 20 or 30 keV. The aim of these observations was to characterize the spherulites microstructure and to describe fracture mechanisms respectively.

2.2.4 Electron Back-Scattered Diffraction (EBSD)

EBSD analyses were made with an Oxford Instruments EBSD Symmetry camera (Abingdon-on-Thames, UK). The parameters used to perform the EBSD were a tension of 20kV, a diaphragm size of 120 µm, the high current mode selected, the exposure time was set to 9 ms. The EBSD data were post-processed with 'Channel 5' software (Oxford Instrument).

2.2.5 Energy Dispersive X-ray Spectroscopy EDXS

To ensure that the composition of each sample was consistent with the desired one and that no evaporation of elements had occurred during the master alloy's

processing, the composition of all the cast ingots was controlled by EDXS X-max 50 mm^2 Silicon Drift Detector (Oxford Instruments, High Wycombe, UK) in SEM at an acceleration voltage of 5 keV. Moreover, three maps with Ti, Cu, Zr and Pd atomic distributions were performed on one spherulite of the BMG, each map measuring 22 µm x 16 µm. The maps were performed at the center of the spherulite, intermediate part and at the spherulite/matrix interface.

2.3 Mechanical characterization

2.3.1 Compression tests

The compression tests were conducted on 6 cylindrical samples of 3mm diameter and 5 mm height. The tests were performed on an INSTRON 5967 machine (Nordwood, USA) with an optical extensometer and a 30kN load cell. The deformation rate was fixed at $1.4x10^{-4}$ s^{-1}.

2.3.2 Tensile tests

Tensile tests were performed on the same machine used for the compression test (INSTRON 5967). To avoid premature specimen's failure in conventional jaws, a self-aligning fixture (with an additional degrees of freedom) was used and the edges of the specimens were threaded for this test. The test specimens were machined in a dog-bone shape, with a working part of 5mm long (for a total length of 20 mm) and a diameter of 2.46 mm. The test speed was set to 0.058 mm/s.

2.3.3 ISO14801: Load to failure tests on dental implant representative sample

Mechanical characterization and evaluation of the load to failure of reference implant-representative samples (call hereafter REPSAMPLES) were evaluated on a BOSE ELF3300 testing machine (New Castle, PA, USA) following the geometrical specifications of ISO 14801 (displacement rate of 5 mm/min)[11]. The geometry of the samples consisted in an outer diameter: ⦸ 2.8 mm and ⦸ 2.3 mm in the deeper thread. They were embedded in a resin having a Young's modulus of 7 GPa after polymerization (Rencast© Resin, HUNTSMAN) and with 3 mm of non-impregnated threads simulating bone resorption. Hemispherical caps were sealed onto the top of the sample in order to ensure a constant lever arm of 11 mm on each assembly for

mechanical testing. Which is achieved through a force applied at 30° to the longitudinal axis of the implant (picture of the assembly visible in Figure 10).

2.3.4 ISO14801: Fatigue tests on dental implant representative sample

Fatigue tests were performed using the same machine and geometry described in the previous paragraph. REPSAMPLES were tested in air at room temperature with a frequency of 15 Hz. A sinusoidal load between 0.1 and 1 times the maximum applied load was used. The fatigue limit was set to 5 x 10^6 cycles in this case, if no failure occurred at 5x10^6 cycles, then the maximum load was increased by 10 N. The test was following the IACS UR M53 Appendix IV standard. The fatigue fracture surfaces were observed by SEM in order to identify the fracture initiation and behavior.

2.3.5 Toughness evaluation: Single Edge V Notched Bending (SEVNB)

To determine the toughness of the material, a method known and considered to be accurate and reliable for materials with brittle behavior was used, namely the Single-Edge V-Notched in Bending (SEVNB) method [15].

For this purpose, 3 samples with a rectangular cross-section were notched with a femtosecond laser to a known depth with 16 passes of 50 µJ infrared ultra-short laser pulse. The use of the laser leads to much finer and sharper notches than can be obtained with a more traditional method such as razor notching [16]. The dimensions of the specimens were as follows: length 25 mm, width 2 mm and thickness 4mm. The notch length was comprised between 210 and 250 µm with a very sharp notch tip radius (around 5 µm). The specimens were tested at 0.5 mm/min on a 4-points bending test until failure. From the load to failure values, it is possible to calculate the critical stress intensity factor K_{IC} by knowing the notch length:

$$K_{IC} = \frac{3F(L-l)}{2bW^2}.Y.\sqrt{a} \quad (1)$$

Where *L* and *l* are the outer and inner spans (21 and 10mm, respectively), *b* is the thickness of the samples (4mm), *W* is the width (2mm). *F* is the load to failure in N and a is the notch length in mm (measured precisely for each sample).

Y is a constant defined by the following formula:

$$Y = \left(\frac{1.1215\sqrt{\pi}}{\beta^{\frac{3}{2}}}\right).\left[\frac{5}{8} - \frac{5}{12}\alpha + \frac{1}{8}\alpha^2\beta^6 + \frac{3}{8}e^{-6.1342\alpha/\beta}\right] (2)$$

With $\alpha = \frac{a}{W}$ and $\beta = 1 - \alpha$ (3)

2.4 Electrochemical characterisations

2.4.1 Macroscopic corrosion behavior

The assembly of the electrochemical micro-cell is based on the principle of the classic

a three electrodes electrochemical cell for voltammetric analysis, using a Gamry instrument 600+ potentiostat (Philadelphia, Pennsylvania, USA) with graphite rod as the auxiliary electrode and an Ag/AgCl ($E_{Ag/AgCl}$= 224 mV vs Standard Hydrogen Electrode at 25°C) as reference electrode. Prior to electrochemical measurements, both BMG and reference samples (TA6V) rods of 5mm in diameter were polished using abrasive papers down to #2400 in order to obtain a smooth surface before the test. In order to expose only a known surface of the rod (rod 's section = 19.63mm^2), the rod is surrounded by an insulating and waterproof sheath. An aerated ad neutral saline solution composed by 0.9 % of NaCl (pH: 7.4) at 37°C was used as the electrolyte. This solution was chosen as it is recommended in the ISO 10271 standard, dedicated to the corrosion test methods for metallic materials used in dentistry. As the susceptibility of passive material to localized corrosion is directly affected by the presence of chloride ions, saline solution is an adequate electrolyte to measure such a property.

Before plotting the polarization curves, open circuit potential (OCP) measurements were performed during 6h to achieve the steady-state in the NaCl solution. Then, a linear polarization with a scan rate of 0.17 mV/s, from −0.5 V vs Ag/AgCl to +1 V vs Ag/AgCl The corrosion potential (E_{corr}), the pitting potential (E_{pit})and the passive current density were estimated from the polarization curves. After the tests, the surfaces were observed at SEM, to characterized the corroded surface morphology. The curves corresponding to this test are already published in [17].

Complementary test was performed on a sample with another surface preparation to highlight the nucleation of the pitting process. The samples were polished using

abrasive papers down to #2400 and by a final step with OP-S 75% and H_2O_2 as in 7.2.1.1 for microscopic observations. Then, the corrosion potential was measured during 30 min to stabilize the sample's potential in the saline solution. Finally, cyclic polarization was performed, with a scan rate of 0.17 mV/s from anodic -0,2 V vs Ag/AgCl to 0,5 V vs Ag/AgCl with a maximum of current density of 0.5A/cm^2 to just start the pitting phenomenon and then the potential was reversed with the decrease of the current density.

2.4.2 Local electrochemical behavior

The local measurements are based on the same principle as described in the previous paragraph, the main difference is the reduction in size of the measuring area (working electrode). This technique makes possible the electrochemical analysis of selected, small areas (about 50 µm in diameter maximum) such as a single heterogeneity size. It is possible to study these very small areas via the preparation of tight stretched glass capillaries (with silicone gasket at the end of the capillary in this study). To do so, capillaries of 1mm diameter in borosilicate were hot stretched with a capillary stretching machine [18]. Then, the ends of the capillaries were hand-polished (with a sheet of wet SiC 1000 to have a surface at 90° to the long axis of the capillary) to have a disc shape for the opening of the capillary. The diameter of the capillary opening corresponds to the metallic glass area exposed to the electrolyte comprised between 20 and 50µm (controlled by optical microscopy). To ensure a good contact between the sample and the capillary and ensure the water tightness, silicone gasket is obtained by repeating back and forth with the end of the capillary at 90° of a silicone layers, between each back and forth, ethanol and water are injected successively with a syringe into the capillary to ensure its opening. The capillary is considered ready for measurement when the silicone seal is about 30µm on each side of the capillary. Then, the capillary is put in place and filled by the electrolyte, as well as the electrochemical cell containing the working electrode and the counter-electrode (here Platinum). The reference electrode (Ag/AgCl) is outside the cell, but connected to the assembly by a pipe filled with electrolyte opening into the cell.

The local electrochemical equipment was connected to a Gamry Instrument Reference 600+ potentiostat (Philadelphia, Pennsylvania, USA). Prior to electrochemical

measurements, BMG samples were ground using abrasive papers, followed by colloidal silica suspension as previously described in order to see clearly the spherulites on the 5 mm in diameters BMG rods. The NaCl 0,9% solution was also used for this test. Before potentiodynamic polarization measurements, OCP measurements were performed during 30 min to stabilize the samples in the saline solution. Finally, linear polarization was performed, with a scan rate of 0.17 mV/s from anodic -0,4 V vs Ag/AgCl to 0,8 V vs Ag/AgCl. The corrosion potential (E_{corr}), the pitting potential (E_{pit}) and the passive current density were estimated from anodic polarization curves. After the tests, the surfaces were observed with optical microscopy to check the change of the surface state. 6 measurements on the amorphous matrix and 6 measurements on the spherulites (measurement considered in relation to the OCP values).

3 Results

3.1 Microstructural observations

3.1.1 Optical microscopy

With the polishing protocol set up for this study, the 'spherulites' are easily visible under light microscopy as shown in Figure 1. Most of them exhibit a spherical shape, with a clear interface with the amorphous matrix. Their diameter is relatively large, reaching several hundreds of µms. At high magnification, some details of the microstructure can be seen: in the center of the spherulites, very fine needles can be seen, looking like dendrite or martensitic phases. This could be due to a preferential growth direction of theses structure from the core to the periphery of the spherulites. Closer to the interface with the matrix, the microstructure of the spherulite becomes less clear. These observations show that the spherulites are likely crystalized. Moreover, two different grey levels in the spherulite on the right picture can be distinguished, which could correspond to different crystalline phases or crystallographic orientations contrasts.

3.1.2 Statistical analysis of mean spherulite diameter

In this study, the mean diameter of the spherulites could not be defined through 3D measurements and only 2D images of the samples were available. X-Ray Tomography was indeed tested, but there was no density contrast between the spherulites and the amorphous phase. Saltykov's method [19] was performed on these 2D observations, with statistical coefficients to correct the measurement's bias and obtain an average diameter closer to reality. The results shown in Figure 2 suggest a mean diameter around 150 µm, some spherulites being of several hundreds of microns in size. Moreover, the observations did not show any preferential location of the spherulites in the sample (no difference between the core and the periphery of the rods).

3.1.3 XRD Analysis

In most studies involving metallic glass [20–22], XRD is used as a mean to check the amorphous state of the parts before conducting further experiments. This conventional method was used on a rod of the TiCuZrPd grade, which after polishing exhibited a lot of spherulites in optical microscopy (around 40 spherulites on a surface of around 19.6 mm^2, which is around 2 spherulites by mm^2, see Figure 1). The diffractogram shown in Figure 3 presents only broad halos with the absence of well-defined peaks. Thus, it could be considered as characteristic of an amorphous metal alloy, even though the presence of numerous spherical defects was noticed on the sample's surface. The surface percentage occupied by spherulites on this sample has been calculated and it is equal to 1.2%, which represents a low fraction of global surface thus too small to be detected by XRD. This sheds a light on the limit of standard XRD to detect spherulites in such BMG systems.

3.1.4 Scanning Electronic Microscopy (SEM)

Figure 4 gathers several SEM pictures of spherulites at different magnification. The observations of SEM pictures suggest three successive distinguishable zones of the spherulite's microstructure. From the center to the periphery:

(1) well delimited needles/slats that go in all directions of the space, which were already observed by optical microscopy (Fig.1), the three grey contrasts being

either due to differences of composition or to different orientations ('channelling' of the electrons),

(2) then the microstructure refines as a transition phase with very small grains then large and elongated grains with different grey contrasts (different orientations or compositions),

(3) finally, the presence of a thin shell with an average thickness of 3.7 µm (±1.2 µm). consisting of columnar nano-grains.

3.1.5 Electron BackScatter Diffraction (EBSD)

Due to the complex composition of the alloy and of the out-of-equilibrium processing method, the exact phase(s) present are not known. However, it was possible to index the major portion of the spherulite grains by declaring a simple cubic crystalline phase with parameters corresponding to a B2 CuPd phase, with a Face-Centered Cubic (FCC) lattice type and a space group Fm-3m (225). The dimensions of the lattice are a = b =c =3.766 Å, α=β=γ = 90° and the unit cell volume is 53.41 $Å^3$. EBSD is not a phase identification tool and here it is only possible to conclude that de main crystalline phase of the spherulite is probably FCC with a lattice parameter close to 3.766 Å. The map shown in Figure 5, positioned on a spherulite's quarter, indicates that the grains are well indexed and mostly oriented towards the [0 0 1] planes. The map of local disorientation indicates values between 0.5 and 2° of disorientation (with a maximum occurrence at 0.6°). Moreover, it can be seen that the shell has not been indexed either probably because the size of the crystals is too small or it is constituted by another crystalline phase.

3.1.6 Energy Dispersive X-ray Spectroscopy (EDXS)

Figure 6 shows the atomic surface distributions superimposed with SEM images of the microstructure of the spherulites. A spatial atomic segregation of the constituent elements of the alloy can be seen on the "needle" part at the center of the spherulite. Three phases may be distinguished from this map (top left): Palladium rich lamellae, an intermetallic (interdendritic) Zirconium rich phase (light grey) and finally another intermetallic CuTi rich phase (dark grey). On the other maps, this segregation is only slightly or not visible at all. It leads to the conclusion that segregation is occurring mainly at the center of the spherulite whereas the outer part is more homogeneous in

chemical composition. At the interface with the amorphous part, no segregation can be seen.

3.2 Mechanical characterization

3.2.1 Hardness Vickers measurements

Table 1 shows average values of hardness in the spherulites and in the amorphous matrix. The amorphous matrix has a much higher average hardness (556 HV) than the spherulites (307 HV). Figure 7 illustrates the difference in indent size between amorphous matrix and spherulites, which is in line with the values measured. Moreover, in some cases in the spherulites some lines can be seen that look like crystalline-plasticity slip bands, which can be found in common crystalline metallic materials. These features are not noticed in the amorphous matrix.

3.2.2 Compression and tensile tests

Mechanical properties (Young's modulus, compressive strength, elastic and plastic strains, load to failure and fatigue limit) obtained from the overall set of mechanical tests are summarized in Table 2. Several compression stress-strain curves can be seen in Figure 8. The curves are superimposed on the elastic part (with an elastic deformation of about 2%), with a small dispersion on strength but with variations in plastic strains at failure from one specimen to another (between 0.2 and 0.7%). The compressive strength value calculated from these curves is on average equal to 2GPa and Young's modulus is about 105 GPa. The picture of the compression fracture surface in Figure 8B has a very matt appearance which corresponds to a propagation of the crack in mode II, in line with a surface fracture angle of around 45° observed here for every sample. The origin of the fracture is not apparent and no spherulites are visible.

Tensile stress-strain curves of the BMG for four specimens are also given in Figure 8C. The first conclusion to be extracted from these curves is that all specimens except one show brittle fracture before plasticity. The mechanical strength is ranging between 1075 and 1820 MPa, a very large dispersion. It is interesting at this point, to see that the sample 4 revealing a very short plateau, thus likely (limited) plasticity, broke at the highest stress (1820 MPa), which is not far from the compressive yield strength.

Fracture surfaces of all the tensile specimens exhibit spherulites. The picture of the tensile fracture surface is very different from the compressive fracture surface. The starting point of the crack appears to be two large, adjacent spherulites. The crack then propagated in mode I in the rest of the specimen.

Figure 9 illustrates the ability of spherulites to deform in compression. Figure 9A shows an area of the sample (not on the fracture surface but on one polished side of the specimen) before and after the compression test. It can be clearly seen that the spherulite has deformed plastically under the compressive stress through crystalline-plasticity slip bands (white arrows). Shear bands (red arrows) can be seen around the spherulite in the amorphous matrix, oriented perpendicular to the compression axis. On the high magnification picture, these multiple small shear bands tend to gather into a single shear band when moving away from the spherulite. These observations lead us to believe that the spherulites deformed first, which led to the premature formation of shear bands in the amorphous matrix around them. These observations will be addressed again in the discussion of the article.

3.2.3 Load to failure: standard ISO14801

Figure 10 shows the stress-strain-displacement curves up to rupture of 6 REPSAMPLES, tested according to ISO 14801. The loading configuration of the ISO 14801 leads to a bending mode of the implants (the tensile and compressive side of the specimen is given on the fracture surface shown in Figure 10). It can be seen that there is a high variability of maximal load to failure between all these specimens, ranging from 366 to 744 N. However, all of them except one broke in the elastic range and therefore did not show any plasticity (the curvature in the load-displacement being related to the deformation of the acrylate resin). On the fracture surface shown in Figure 10, the starting point of the crack is clearly visible as a large spherulite on the tensile surface of the specimen. This is probably one of the worst situations that can be encountered in this test (a large spherulite at the tensile side). The rest of the surface of the specimen has a very matt appearance which corresponds to a fast fracture zone (stage II on the picture) with a last fracture of the compressive ligament (denoted III). The crack does not pass through the spherulites but around them, which shows a decohesion between

the matrix and the spherulites at the interface. Overall, fracture occurs in mode I, i.e. with a crack propagation perpendicular to the maximal tensile stress.

3.2.4 Fatigue test: standard ISO14801

Figure 11 shows the S-N curve for the REPSAMPLES. The fatigue limit of this BMG is estimated to be 300N, which is high for a biomedical metal alloy considering the small dimension of the samples tested here [24,25]. There is some dispersion in the results, again related to the presence of the spherulites inside the pieces. Figure 11B shows a typical fracture surface: the starting point of the crack propagation on the tensile side is associated to a spherulite of around 500µm in diameter near the surface. The crack propagated in fatigue mode I (stage I in the picture) for some time and then a fast fracture mode appears (stage II) with a surface feature similar to the one observed during the load to failure tests. As for the static tests, a decohesion between matrix and spherulites can be seen. From this overall set of experiments, it is clear that spherulites can act as critical defects in tension and as nucleation sites in fatigue.

3.2.5 4-point bending test – SEVNB

The results of the 4-point bending test on notched samples are summarized in Table 3. With the data obtained thanks to equations (1) and (2), we were able to calculate a K_{IC} ranging between 32 and 42 $MPa\sqrt{m}$.

3.3 Corrosion resistance characterisation

3.3.1 Macroscopic corrosion behavior

The polarization curve of the BMG from -0.5 to 1V vs Ag/AgCl in a 0.9% NaCl solution obtained after 6 hours of immersion is available in [17] where the BMG is compared to a TA6V benchmark. The cathodic branch exhibits the same shape for the two materials and it is linked with the oxygen reduction occurring on both surfaces. Nevertheless, the TA6V has a lower current density on the cathodic part. The value of the corrosion potential E_{corr} of TA6V is lower than that of TiCuZrPd suggesting a difference in reactivity between both materials. In the anodic branch, the current density then increases with the potential for both alloys to achieve a passivation plateau. Both materials behave as a passive material and the 6 hour of immersion seems sufficient to grow a stable passive film. Conversely to TA6V, the polarization curve of the TiCuZrPd

BMG exhibits an abrupt increase in current density at a potential of around 360 mV vs Ag/AgCl which corresponds to pitting potential (E_{pit}). Figure 12 A and B shows SEM pictures of the surface of the samples tested in electrochemistry. The entire surface of the TiCuZrPd sample is damaged by the test and covered with corrosion products. Numerous pits and crevices are observed on the overall tested surface. However, it seems that the pitting corrosion sites are not totally random and a specific pattern may be observed suggesting that there are preferential nucleation sites. These nucleation sites might correspond quite well to the position, size and morphology of the spherulites. To demonstrate this finding, a less severe test was performed.

3.3.2 Local electrochemical measurements

Figure 13B shows the OCP curves of the entire sample (blue curve), and some corresponding to local measurements on spherulites (red curves) and matrix (black curves). The first information is that all the curves reach a stable potential value between 0V and 0.2V vs Ag/AgCl of potential after immersion of 30 minutes. Independently of the location of the measurement, the value of OCP after 30 min is almost the same for all the measurement.

For the potentiodynamic curves (Figure 13A), only three curves have been shown (for ease of reading) but many measurements have been made on the amorphous matrix and on the spherulites. The cathodic parts of the curves are close from one measurement to another regardless of the targeted area. The values of E_{corr} for the global TiCuZrPd is around 0V vs Ag/AgCl and those corresponding to local spherulites measurements are in average close to 0V vs Ag/AgCl or slightly lower. For the matrix's ones, there is a little more dispersion, but the average value is also around 0V vs Ag/AgCl. Then the anodic branches are increasing following a passivation plateau shape more or less long before a sudden increase, corresponding to pitting phenomenon. Interestingly, the electrochemical behavior is similar whatever the location of the measurement.

Two examples of optical microscopy observation after the local measurements on spherulite and amorphous matrix are displayed in Figure 14. There are in accordance with the previous curves. Indeed, on both pictures, a dark ring around the capillary

position consisting of corrosion products deposition is observed. The appearance of the sample's surface reaction after measurements seems to be identical on both areas.

Figure 15 shows two SEM pictures of the sample surface after a cyclic polarization test with a low threshold (low enough to identify the starting point of the pitting). Spherulites are not preferential starting points for pitting. It seems rather that the starting point is on areas that appear random from the amorphous and spread. Furthermore, the spherulite shell seems also to preferentially dissolve, creating a void around the spherulite, which can lead to a release of the spherulite into the saline solution.

4 Discussion

Bulk metallic glasses are metallic materials with unique properties that are particularly interesting for the biomedical field. In this context, it has already been shown in the literature that the TiCuZrPd grade is very promising for dental implants manufacturing [10,22]. However, casting defects such as spherulites were not studied in detail so far, while they could alter its properties, particularly mechanical and electrochemical, and therefore may limit its industrialization. This study gives new insights on the characterization of these spherulites and their influence on the properties of use for dental application.

4.1 Spherulite: a complex microstructure

Microstructural observations of spherulites have revealed that they have a fine microstructural core, with lamellae oriented in all directions, which suggests that spherulite growth starts from the center to the periphery, this hypothesis is shared with a previous article [23]. However, the clear interfaces between the spherulite, the surrounding shell and the amorphous matrix are the result of crystallization mechanisms. There is a difference in microstructure between the center of the spherulite and its periphery, the grains are increasingly larger which could be the result of solidification of the same phase with a temperature gradient. Even if the mechanisms of appearance of these spherulites are not clearly elucidated in this article, their observations have allowed us to describe a very particular microstructure which has many points in common with the B2 phase in ZrCu alloys [9,26]. Another

scientific team has already observed the same type of defects in a Zr base BMG [23] but with a laser deposition process. According to their work, the thermal treatment kinetics are involved in the spherulite apparition in the laser heat-affected zone.

In many studies on BMGs, the reference technique to check the amorphous state is X-ray diffraction. Indeed, in most papers, diffractograms show broad halos characteristic of amorphous materials. It is demonstrated here that this technique is ineffective to affirm that a piece is really fully amorphous. A sample with a large number of crystalline spherulites on its surface presented a 'typically amorphous' diffractogram even with a very long acquisition time. This result can be explained by the fact that the surface percentage occupied by the spherulites is too small to obtain a signal, even if they are numerous and large. This result therefore challenges the use of DRX as a method to verify amorphous state and suggests a more in-depth study of the casted samples to assess the absence of crystalline defects whose presence may play a role on many properties of the material.

Spherulites have a hardness 45% less important than the amorphous matrix, in line with literature [27]. Moreover, their distribution appears clearly random. Concerning the hardness difference between spherulites and matrix, it can be easily explained by the fact that the amorphous phase has no crystalline lattice planes on which dislocations can slide and no grain boundaries. Plastic deformation in the amorphous phase results in the formation of very small shear bands (the phenomenon is more visible with higher loadings) [28]. In spherulites, there are defects related to the crystalline organization, including grain boundaries and dislocations (not studied here), which result in easier local plastic formation than in amorphous matrix. This leads to a higher hardness of the amorphous matrix than the crystalline spherulites, as shown in previous article [29]. In addition, EDXS allowed us to illustrate atomic segregation on the central dendritic part of the spherulites. Spherulites consist mainly of a FCC phase (Figure 5), which seems to have lattice parameters close to B2 CuPd phase. On the other side, other phases are present and would deserve further exploration. Some TEM observations were performed on the spherulites and the amorphous matrix. They are not presented here because it would have led to a very long paper and they will be the scope of a specific future publication. The results confirm the above-mentioned

results, the amorphous matrix presenting no atom arrangement and corresponding diffraction FFT was diffuse, which indicates that it is amorphous at the atomic scale. On the spherulite we gathered several FFT patterns showing several crystalline phases. A robust identification of these phases could improve our understanding of their presence and maybe even help to identify the critical parameters responsible for the presence of these defects and thus to avoid their formation. It is important to notice that there is really small variation in the atomic composition of the alloy between the amorphous matrix and the spherulites during our EDS measurements, which is coherent with the results found by [23] and thus hinders somehow their detection. For example, X-Ray tomography in contrast mode was not successful.

Spherulites having a large size, a lower hardness and a crystalline nature different from the amorphous matrix, they inevitably have an impact on the mechanical properties of the alloy by inducing a mismatch of their elastic limit.

4.2 TiCuZrPd BMG's mechanical properties

The mechanical characterisation of BMG TiCuZrPd rods enabled us to determine the main mechanical properties of the material. As already mentioned in previous literature, this BMG does not present a high Young's modulus but a very high mechanical strength [30]. A modest value of Young's modulus for a metal might be interesting for implant applications, since it may limit stress-shielding phenomena [31]. Although showing a certain ductility in compression, this BMG exhibits a brittle fracture behavior in tension as already mentioned by [2]. In a large number of papers on BMGs, the compression test is chosen because of its simplicity and the potential of making experiments with a low amount of material on small samples. On the other hand, the fracture surfaces observed for compression lead us to believe that this test is not completely suitable for evaluating the mechanical properties of a metallic glass, especially if they are to be used with other loading configurations in practice (as it is the case for dental implants for example). The presence of spherulites cannot be observed on the fracture surface of samples tested in compression, while they are clearly visible in tension. It is thought that the visibility of spherulites on the surface of the tensile specimens can be explained by the different modes of failure between

compression and tension. In tension, mode I is predominant and this will enhance the influence of the defects on the properties by favoring the nucleation of cracks at the interface by stress concentrations at the spherulite/amorphous phase interface [5]. The larger a spherulite and the closer it is from the sample surface, the more premature the rupture (see surface fracture of figure 8). On the other hand, in compression, mode II will be promoted and it is less sensitive to presence of defects. In tensile samples, the spherulites come visible at the fracture surface since cracks can initiate from the spherulites and propagate at the interface with the amorphous region. In compression, the spherulite first plastically deform and create the premature formation of shear bands (see figure 9). The spherulites deformation may be the reason why some plasticity can be seen on the compressive stress-strain curves and why they are not visible on the fracture surface[6]. In any case, with spherulites of several hundred of micrometers diameter, the spherulites seem to be deleterious for the mechanical properties in both solicitation mode.

4.3 Estimation of the critical size defect

Taking the strengths obtained in tension and the size of the largest spherulite present on the fracture surfaces of each tensile specimen can allow estimating the toughness, for the hypothesis is that they are the critical defect at the origin of the failure. Using the standard equation of the K_{IC} calculation for simple configurations considering the stress at failure, σ_r, and the defect size a [32] gives:

$$K_{IC} = \sigma_r \times \sqrt{\pi \times a} \qquad (4)$$

The spherulite's radii measured on the surfaces are between 110 and 255µm and the stresses at failure are between 1073 and 1820 MPa. Thus, the toughness K_I can be estimated between 30 and 36 MPa$\sqrt{m}$, which is in line with the K_{IC} measured by SEVNB (Table 3). This confirms that the spherulites acts as stress-concentrators and defects and are thus to a certain extent detrimental to the strength.

The lack of reproducibility of the fatigue results on REPSAMPLES does not allow us to really conclude on the fatigue limit of this alloy, even if among the curves there is a high load at breakage (more than 600N) and a fatigue limit around 300N. These properties are still promising for a biomedical alloy, although their dispersion is a

concern. Fracture surfaces showed spherulites close to the surface in tension, which visibly leads to spherulite matrix decohesion and thus probably to a critical and premature crack initiation. There is a wide dispersion in the results which could be related to the size of the spherulite and/or their distance from the surface in tension.

The mean value of the toughness measured by the SENVB test was of K_{IC}=36.2 (±4.2 $MPa\sqrt{m}$). As far as we know, the toughness value of this alloy has not yet been published so it is impossible to compare our results with those of the literature but this is in line with what we approximate in tension. From this value(s) of K_{IC} and the yield stress of the material measured in compression, it is possible to evaluate the dimension of the plastic (process) zone, given by [32]:

$$\mathrm{d}_y = \frac{K_{\mathrm{I}c}^2}{\pi\sigma_e^2}$$

Where d_y is the size of the plastic zone in m, K_{IC} the toughness in $MPa.\sqrt{m}$ and the yield stress in compression in MPa.

The corresponding plastic zone size before failure should be comprised between 100 and 180µm. It is accepted that if the critical defect size in a material is larger than the size of the plastic zone, then there is fracture before plasticity [32]. According to Figure 2, spherulites with a diameter greater than 200µm are present in the material, i.e. larger than the plastic zone diameter. These large spherulites may be few in number, but their presence can easily explain the early brittle fractures that have been observed in tension and on the ISO14801 standard assembly. In this case, spherulites have been shown to have a negative influence on the mechanical properties of the alloy [6]. However, a control of the size of these spherulites and therefore their reduction to below the size of the plastic zone can be a perspective for the optimization of this alloy. For example, by varying the heating temperature, the diameter of the rods during casting and/or the cooling rate, one may control (limit) the size of the spherulites, so that the largest would be below 100µm, which would certainly insure plasticity before fracture, even in tension and would limit the risk of fatigue crack growth under cyclic loading.

4.4 TiCuZrPd BMG: Corrosion behavior

Since EDXS has shown that spherulites are of the same average chemical composition or almost the same as the amorphous matrix, it was important to know whether their presence has an influence on the corrosion resistance of the alloy. In the dental domain, the corrosion issues in the oral environment are of prime concern and thus the electrochemical properties of the materials of the future implant must be fully understood. After an overall electrochemical study of TiCuZrPd, it appears that this is a passivable material. This ability to form a protective oxide layer on the surface is requested in the dental environment because it protects the implant from the external environment and thus ensures a certain longevity. However, in the case of TiCuZrPd, pitting corrosion is observed at a relatively low potential [22]. The pictures of the sample's surface after the test are in favor of the involvement of spherulites in the pitting mechanism, hence highlighting the interest of carrying out local electrochemical study. Several possibilities exist to explain the role of casting defect on the phenomenon of pitting of TiCuZrPd BMGs. The first one is that the spherulites by their crystallographic organization can modify the spherulite's potential compared to the amorphous matrix. In that case, it is possible that a local galvanic coupling will be created between the matrix and the spherulite, because all the specific conditions will be gathered (immersed in solution, one part more noble than the other and a direct electric transfer between both parts). It is important to note that the curves from local measurements are in fact numerous and sometimes not very reproducible, this measurement technique is difficult to implement and really very sensitive to the slightest change, it is nevertheless possible to draw trends. However, local electrochemical measurements indicate that in the tested saline conditions, the OCP measured after 30 min is similar for amorphous matrix and spherulite. Furthermore, the electrochemical behavior of both locations is also very similar. Consequently, these findings seem to invalidate the galvanic coupling theory. Another hypothesis for the role of the spherulite which was evidenced Figure 15. Indeed, the interface area between the amorphous matrix and the spherulite, (the small shell observed by SEM) seems to be more sensitive to dissolution than the matrix and the spherulites themselves. Consequently, as proposed in [17], the saline solution attacks

preferentially the shell structure maybe because of a small difference in chemical composition. The propagation of the corrosion damage may allow the penetration of the chloride ions under the spherulite and then provoke local crevice corrosion. However, it is important to mention that deviation of corrosion behavior was noticed during the local electrochemical test on amorphous matrix and that for short pitting test, corrosion attacks were mainly observed in the matrix. Both findings indicate that the chemical composition of the BMG is probably not homogenous on the overall surface. Consequently, the pit nucleation phenomenon is not strictly stochastic but depends of the local chemical composition of the matrix.

4.5 Spherulite as reinforcement in the BMG?

The work presented in this article does not allow to conclude on the origin and exact nature of spherulites. However, there is some literature on so-called 'composite' metallic glasses with an amorphous BMG matrix and a crystalline reinforcing phase, which should in principle provide ductility to BMGs. There are many different grades, but the one that has attracted our particular attention are the CuZr based grades with the addition of Ti or Al as a doping element to increase the GFA. In 2009, Pauly and co-workers[7] reported the presence of a B2 phase (CuZr) which forms spontaneously when the rod is cooled. The proportion of this phase is highly dependent on the diameter of the part and therefore on the cooling rates. The B2 phase is represented by crystalline spheres not randomly distributed in the rods (which aggregate in the center part of the rods). They also specify that the B2 phase can be transformed into the so-called martensitic B19 phase (with highly visible needles) under the effect of stresses, composition or cooling speed. This transformation from phase B2 to B19 is known and has been shown to bring plasticity [26]. The overall difficulty of BMG is to have a small proportion of B2 distributed in a totally random way in the rods and which induces plasticity without reducing mechanical resistance. Another team demonstrated that crystalline spheres act as strong barriers for the rapid propagation of shear bands [5,6]. Using a finite element model, they specify that if the spherulites are monodisperse and randomly distributed, then the strain field are more uniform and shear bands can interact and multiplied, which should be beneficial for plasticity. Kim et al. [9] give some clues on the origin and growth of this B2 phase, and mention

polymorphism crystallization induced by “reduced interface kinetics of solid/liquid interface”. They could also see a shell around the spherulites (about 1µm width), as we observed in the present work. The growth of the spherulites seems to continue until the glass around it solidifies.

These elements could link the appearance of spherulites with the presence of oxygen or other pollution elements during casting or perhaps a too low purity of the raw material. Pollution by third-party elements, even at very low contents, could act as a starting point for nucleation. Another explanation could be the spontaneous formation of phase B2 CuTi due to an insufficient cooling rate to freeze the entire bar in an amorphous state [33].

The crystal defects observed in the TiCuZrPd grade are of large diameter and exhibit a complex microstructure. Nevertheless, even if such defects are present, the grade shows very good mechanical properties. Therefore, modifying (decreasing) the size of these spherulites while maintaining their random distribution to improve the mechanical/corrosion resistance properties and provide ductility, as is the case with BMG's ZrCu, can be a strong option in the future, to end-up with more reliable, strong and ductile biomedical grade BMG’s.

5 Conclusion

This study demonstrates the presence of heterogeneities in the TiZrCuPd grade, which were not precisely described so far for this composition. These heterogeneities exhibit the shape of large crystalline spheres, up to several hundreds of µm, which nevertheless remain undetected by X-rays. These spherulites do not occupy a large volume fraction, but their large size and much lower hardness than that of the amorphous material are the cause of premature failure of the parts, in particular under tensile loading, where failure occurs before plasticity. The exact nucleation origin of these spherulites during the process would deserve further work and observations of the microstructure of these spherulites is complex, with martensitic needles in the center and a phase identified as CuTi B2 very present, probably with Zr/Ti and Cu/Pd substitutions. Another objective of the paper was to find out whether the presence of these defects was the cause of the modest corrosion resistance of this alloy. It was

shown here that the corrosion and pitting potentials were similar for the spherulites and the amorphous matrix. Therefore, assuming that some corrosion dissolutions initiate on the amorphous matrix, the spherulites, themselves, are probably not the most deleterious to the corrosion resistance. However, the shell at the spherulite/amorphous interface, exhibiting probably a different chemistry, seems to dissolve preferentially in saline solution and have to be controlled.

At the end of this study, it is relevant to ask whether it is more strategic to try to preserve these 'defects' while controlling (decreasing) their size and distribution rather than trying to prevent their appearance, as a controlled crystallization of small particles in a glassy matrix seems to provide ductility and improve toughness in other BMG systems.

Acknowledgements

The authors would like to thank the 'Agence National de la Recherche' (ANR) and its funding within the framework of the ANR-TNT-18-CE91-0005 and of the the Labcom 'LEAD'. The assistance of Professor Moreno and his team with the femto laser notching (SENVB test) by Ultrashort Pulsed Laser Ablation is gratefully acknowledged. Hidemi Kato (Institute for Materials Research, Tohoku University, Sendai) is greatly thanked for his contribution to the material's elaboration and for providing raw materials.

6 Bibliography

[1] S. Yamaura, S. Zhu, K. Abe, G. Xie, Ultrasonic Fatigue of Ti 40 Zr 10 Cu 34 Pd 14 Sn 2 Glassy Alloy, (2014) 56–64.

[2] A. Liens, A. Etiemble, P. Rivory, S. Balvay, J.M. Pelletier, S. Cardinal, D. Fabrègue, H. Kato, P. Steyer, T. Munhoz, J. Adrien, N. Courtois, D.J. Hartmann, J. Chevalier, On the potential of Bulk Metallic Glasses for dental implantology: Case study on Ti 40 Zr 10 Cu 36 Pd 14, Materials. 11 (2018). https://doi.org/10.3390/ma11020249.

[3] Z.F. Zhang, J. Eckert, L. Schultz, Difference in compressive and tensile fracture mechanisms of Zr 59 Cu 20 Al 10 Ni 8 Ti 3 bulk metallic glass, 51 (2003) 1167–1179. https://doi.org/10.1016/S1359-6454(02)00521-9.

[4] Y. Yokoyama, Development of an Automatic Fabrication System for Cast Glassy Alloys, 46 (2015) 893–905. https://doi.org/10.1007/s11663-014-0282-x.

[5] S. Hin, C. Bernard, V. Doquet, Y. Yokoyama, A. Magueresse, V. Keryvin, Influence of as-cast spherulites on the fracture toughness of a Zr 55 Cu 30 Al 10 Ni 5 bulk metallic glass, Materials Science and Engineering: A. 740–741 (2019) 137–147. https://doi.org/10.1016/j.msea.2018.10.061.

[6] C. Bernard, V. Keryvin, Crystalline defects in bulk metallic glasses: consequences on fracture toughness determination and ductility, J. Phys.: Condens. Matter. 32 (2020) 483001. https://doi.org/10.1088/1361-648X/abaa7f.

[7] S. Pauly, G. Liu, G. Wang, U. Kühn, N. Mattern, J. Eckert, Microstructural heterogeneities governing the deformation of Cu47.5Zr47.5Al5 bulk metallic glass composites, Acta Materialia. 57 (2009) 5445–5453. https://doi.org/10.1016/j.actamat.2009.07.042.

[8] Z. Liu, R. Li, G. Liu, W. Su, H. Wang, Y. Li, M. Shi, X. Luo, G. Wu, T. Zhang, Microstructural tailoring and improvement of mechanical properties in CuZr-based bulk metallic glass composites, Acta Materialia. 60 (2012) 3128–3139. https://doi.org/10.1016/j.actamat.2012.02.017.

[9] B.J. Kim, Y.S. Yun, W.T. Kim, D.H. Kim, Microstructure Evolution During Solidification of Cu–Zr–Ti Alloy Forming B2 Phase Particles Embedded in a Glassy Matrix, Met. Mater. Int. 24 (2018) 926–933. https://doi.org/10.1007/s12540-018-0114-7.

[10] S.L. Zhu, X.M. Wang, F.X. Qin, A. Inoue, A new Ti-based bulk glassy alloy with potential for biomedical application, Materials Science and Engineering A. 459 (2007) 233–237. https://doi.org/10.1016/j.msea.2007.01.044.

[11] AFNOR, NF EN ISO 14801 - Médecine bucco-dentaire — Implants — Essai de charge dynamique pour implants dentaires endo-osseux, 2016.

[12] J.-J. Oak, D.V. Louzguine-Luzgin, A. Inoue, Investigation of glass-forming ability, deformation and corrosion behavior of Ni-free Ti-based BMG alloys designed for application as dental implants, Materials Science and Engineering: C. 29 (2009) 322–327. https://doi.org/10.1016/j.msec.2008.07.009.

[13] H.-H. Huang, Y.-S. Sun, C.-P. Wu, C.-F. Liu, P.K. Liaw, W. Kai, Corrosion resistance and biocompatibility of Ni-free Zr-based bulk metallic glass for biomedical applications, Intermetallics. 30 (2012) 139–143. https://doi.org/10.1016/j.intermet.2012.03.015.

[14] H. Ida, M. Seiryu, N. Takeshita, M. Iwasaki, Y. Yokoyama, Y. Tsutsumi, E. Ikeda, S. Sasaki, S. Miyashita, S. Sasaki, T. Fukunaga, T. Deguchi, T. Takano-Yamamoto,

Biosafety, stability, and osteogenic activity of novel implants made of Zr70Ni16Cu6Al8 bulk metallic glass for biomedical application, Acta Biomaterialia. 74 (2018) 505–517. https://doi.org/10.1016/j.actbio.2018.05.020.
[15] M. Turon-Vinas, M. Anglada, Fracture toughness of zirconia from a shallow notch produced by ultra-short pulsed laser ablation, Journal of the European Ceramic Society. 34 (2014) 3865–3870. https://doi.org/10.1016/j.jeurceramsoc.2014.05.009.
[16] R. Damani, R. Gstrein, R. Danzer, Critical notch-root radius effect in SENB-S fracture toughness testing, Journal of the European Ceramic Society. 16 (1996) 695–702. https://doi.org/10.1016/0955-2219(95)00197-2.
[17] A. Liens, B. Ter-Ovanessian, N. Courtois, D. Fabregue, T. Wada, H. Kato, J. Chevalier, Effect of alloying elements on the microstructure and corrosion behavior of TiZr-based bulk metallic glasses, Corrosion Science. 177 (2020) 108854. https://doi.org/10.1016/j.corsci.2020.108854.
[18] F. Andreatta, L. Fedrizzi, The use of the electrochemical micro-cell for the investigation of corrosion phenomena, Electrochimica Acta. 203 (2016) 337–349. https://doi.org/10.1016/j.electacta.2016.01.099.
[19] Saltykov, Stereometric Metallography, 2nd edition, Metallurgizdat, Moscow, 1958.
[20] M. Calin, J. Eckert, L. Schultz, Improved mechanical behavior of Cu–Ti-based bulk metallic glass by in situ formation of nanoscale precipitates, Scripta Materialia. 48 (2003) 653–658. https://doi.org/10.1016/S1359-6462(02)00560-2.
[21] S. Zhu, G. Xie, F. Qin, X. Wang, A. Inoue, Effect of Minor Sn Additions on the Formation and Properties of TiCuZrPd Bulk Glassy Alloy, Mater. Trans. 53 (2012) 500–503. https://doi.org/10.2320/matertrans.M2011281.
[22] N. Hua, X. Hong, L. Lin, Z. Liao, L. Zhang, X. Ye, Q. Wang, Mechanical, corrosion, and wear performances of a biocompatible Ti-based glassy alloy, Journal of Non-Crystalline Solids. 543 (2020) 120116. https://doi.org/10.1016/j.jnoncrysol.2020.120116.
[23] H. Sun, K.M. Flores, Spherulitic crystallization mechanism of a Zr-based bulk metallic glass during laser processing, Intermetallics. 43 (2013) 53–59. https://doi.org/10.1016/j.intermet.2013.06.010.
[24] E. Marchetti, S. Ratta, S. Mummolo, S. Tecco, R. Pecci, R. Bedini, G. Marzo, Evaluation of an Endosseous Oral Implant System According to UNI EN ISO 14801 Fatigue Test Protocol, Implant Dentistry. Publish Ahead of Print (2014). https://doi.org/10.1097/ID.0000000000000151.
[25] E. Marchetti, S. Ratta, S. Mummolo, S. Tecco, R. Pecci, R. Bedini, G. Marzo, Mechanical Reliability Evaluation of an Oral Implant-Abutment System According to UNI EN ISO 14801 Fatigue Test Protocol, Implant Dentistry. 25 (2016) 613–618. https://doi.org/10.1097/ID.0000000000000453.
[26] B. Escher, Stability of the B2 CuZr phase in Cu-Zr-Al-Sc bulk metallic glass matrix composites, Journal of Alloys and Compounds. (2019) 9.
[27] A. Sypien, T. Czeppe, G. Garzel, L. Litynska-Dobrzynska, J. Latuch, N.Q. Chinh, Thermal stability and mechanical properties of the TiCuZrPd glasses with 10, 14 and 20at.% Pd, Journal of Alloys and Compounds. 615 (2014) S108–S112. https://doi.org/10.1016/j.jallcom.2013.12.240.

[28] S. Xie, E.P. George, Hardness and shear band evolution in bulk metallic glasses after plastic deformation and annealing, Acta Materialia. 56 (2008) 5202–5213. https://doi.org/10.1016/j.actamat.2008.07.009.
[29] Y. Wu, Y. Xiao, G. Chen, C.T. Liu, Z. Lu, Bulk Metallic Glass Composites with Transformation-Mediated Work-Hardening and Ductility, Adv. Mater. 22 (2010) 2770–2773. https://doi.org/10.1002/adma.201000482.
[30] P. Gong, L. Deng, J. Jin, S. Wang, X. Wang, K. Yao, Review on the Research and Development of Ti-Based Bulk Metallic Glasses, Metals. 6 (2016) 264. https://doi.org/10.3390/met6110264.
[31] M. Kanto, Radiological Evaluation of the Relationship Between Cortical Hypertrophy and Stress Shielding After Total Hip Arthroplasty Using a Cementless Stem, Arthroplasty Today. (2020) 7.
[32] M.F. Ashby, D. Cebon, Materials selection in mechanical design, J. Phys. IV France. 03 (1993) C7-1-C7-9. https://doi.org/10.1051/jp4:1993701.
[33] W. Song, Y. Wu, H. Wang, X. Liu, H. Chen, Z. Guo, Z. Lu, Microstructural Control via Copious Nucleation Manipulated by In Situ Formed Nucleants: Large-Sized and Ductile Metallic Glass Composites, Adv. Mater. 28 (2016) 8156–8161. https://doi.org/10.1002/adma.201601954.

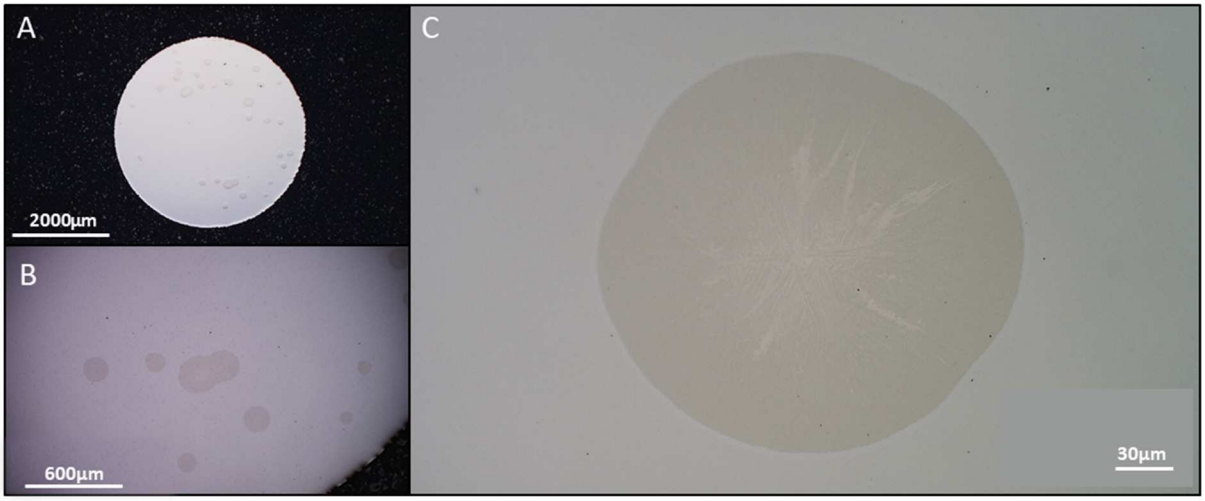

Figure 1: Optical microscopy observations of the TiCuZrPd Bulk Metallic Glass after mechano-chemical polishing with colloidal Silica, showing several spherulites. (A) Global sample appearance. (B) Zoom on the lower part of the rod. (C) High magnification picture of a spherulite.

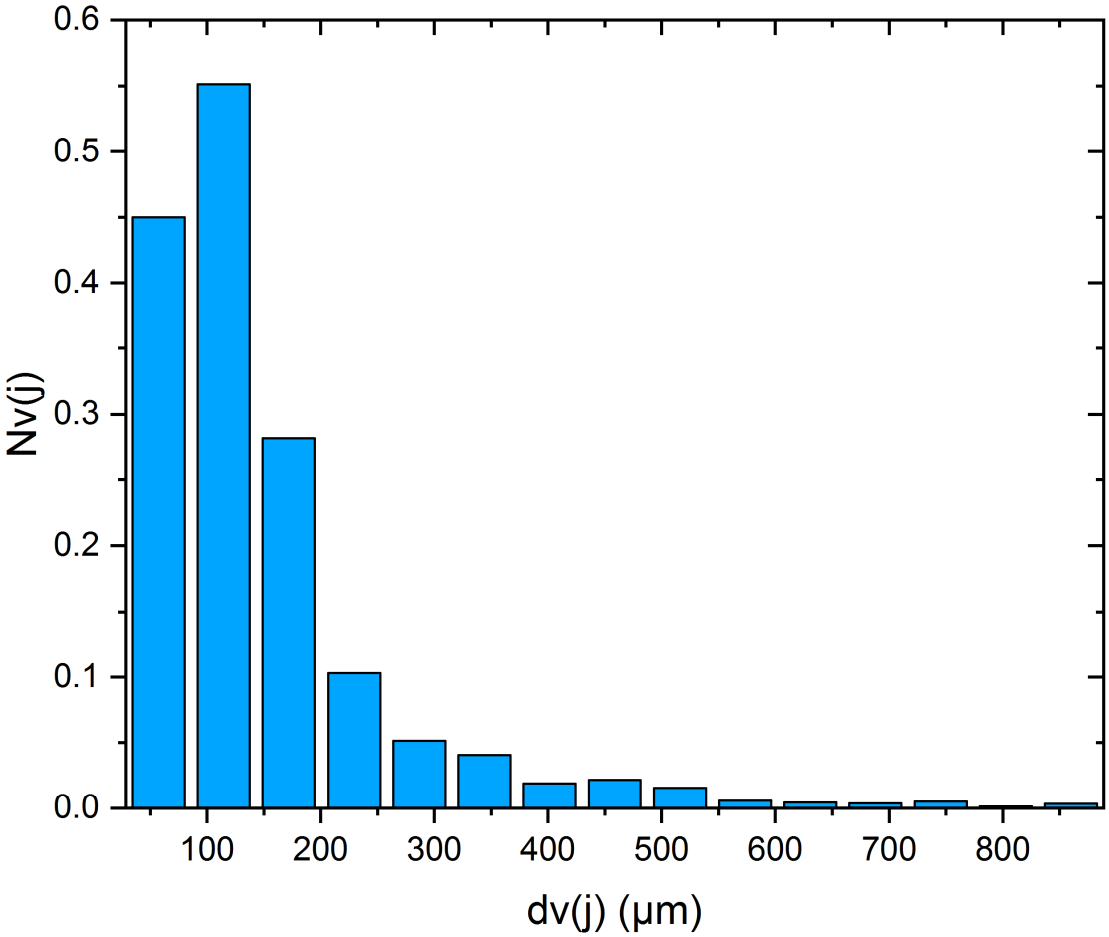

Figure 2: Histogram of spherulites dimensions, analysed by the Schwartz Saltykov method [19].

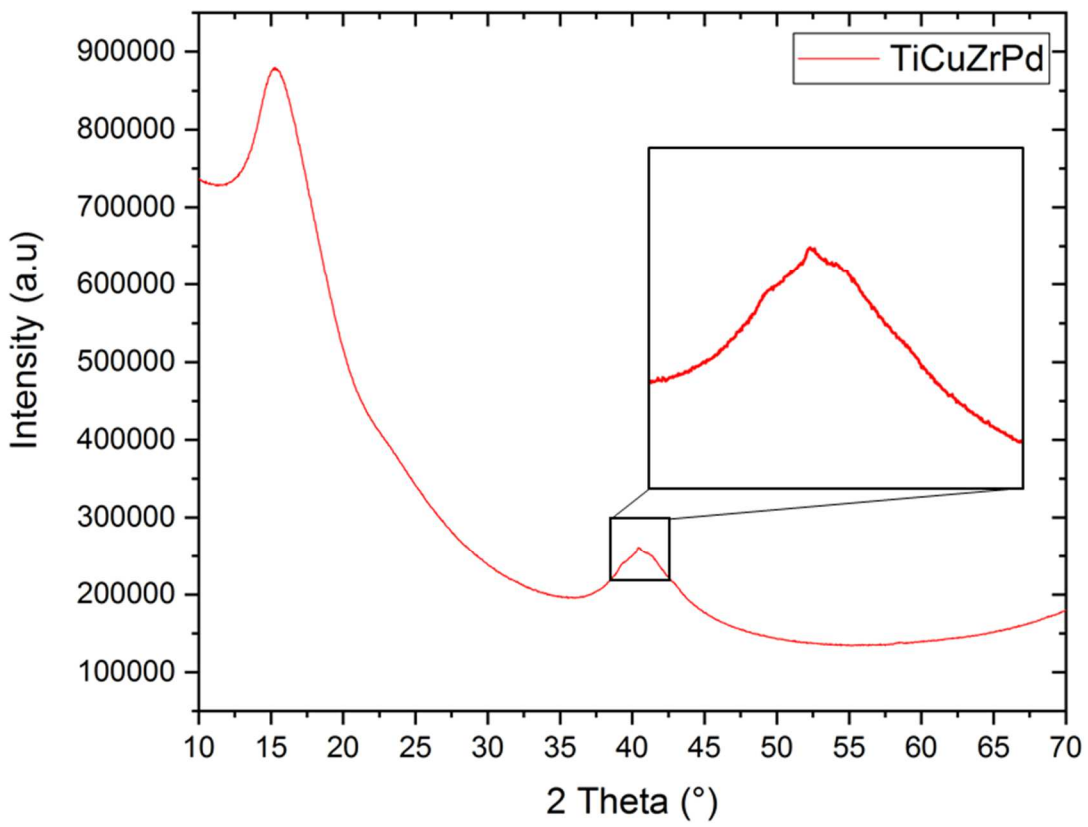

Figure 3: XRD pattern of the TiCuZrPd BMG between 10° < 2θ < 70°. The presence of spherulites is hardly visible, except if a careful analysis of the 41° broad halo is conducted, which may suggest a small crystalline fraction.

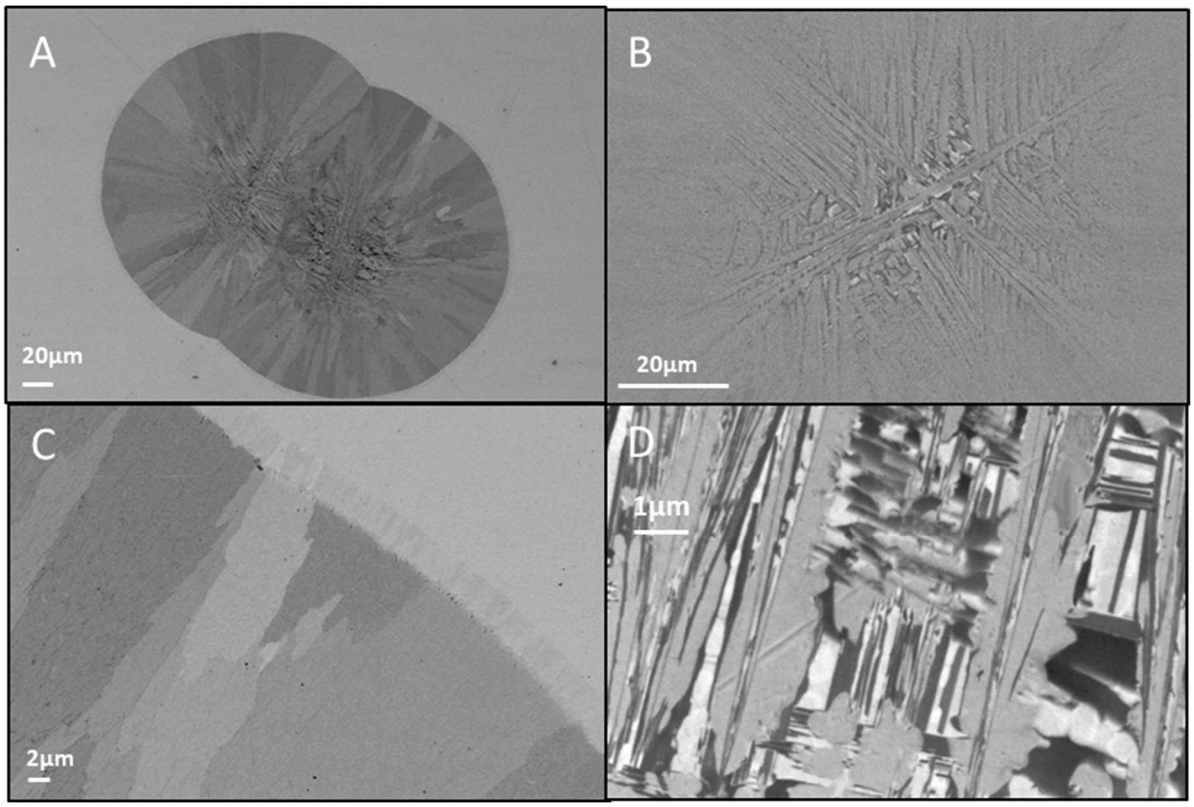

Figure 4: SEM (Back Scattered Electron mode) images of spherulites. (A) Global view of two adjacent spherulites. (B) Higher magnification of the needles in the center part of a spherulite. (C) Higher magnification of spherulite/matrix interface, which shows a 'shell' around the spherulite. (D) Close look at the center of the spherulite, showing different types of needle-shape crystals.

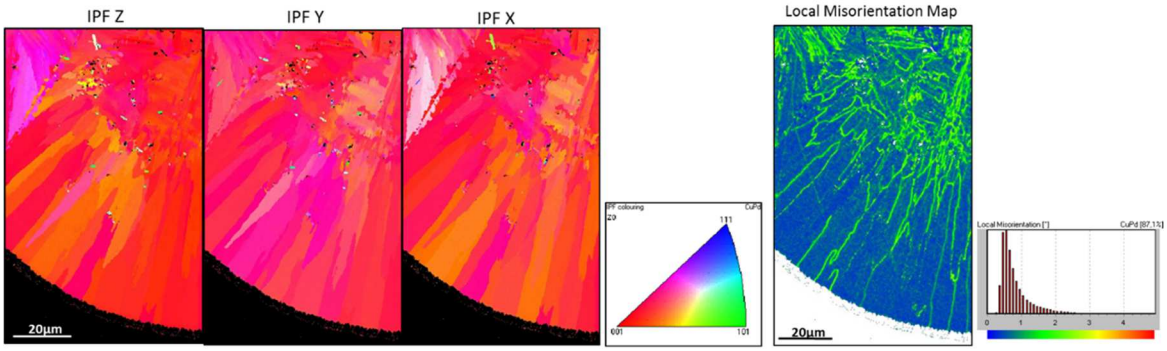

Figure 5: (Left) IPF representations of EBSD map of a part of spherulite. The only visible indexed phase is CuTi. (Right) Corresponding local misorientation map.

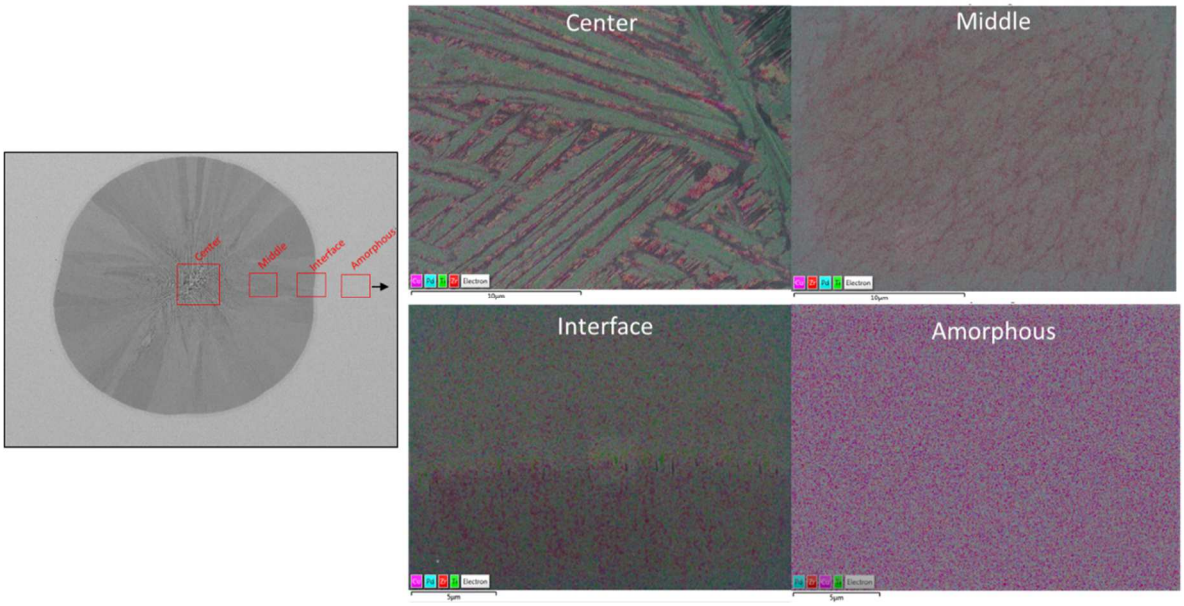

Figure 6: (Left) SEM picture of the spherulite with locations of the different map's spots analyzed by EDXS. (Right) EDXS maps of Ti, Cu, Zr and Pd elements superimposed with SEM pictures at different places of the spherulite.

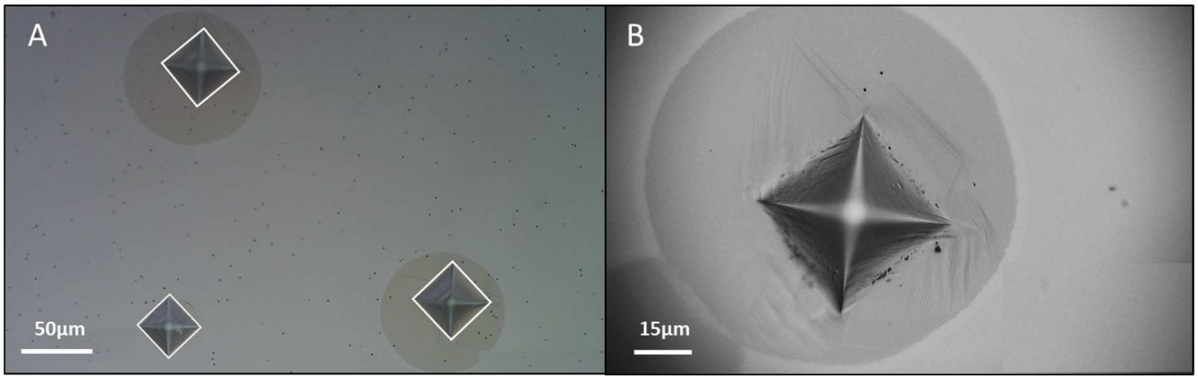

Figure 7 : Observation of Vickers indentations, (A) showing a different Hardness of the amorphous matrix and the spherulites and (B) crystalline plasticity in the spherulite.

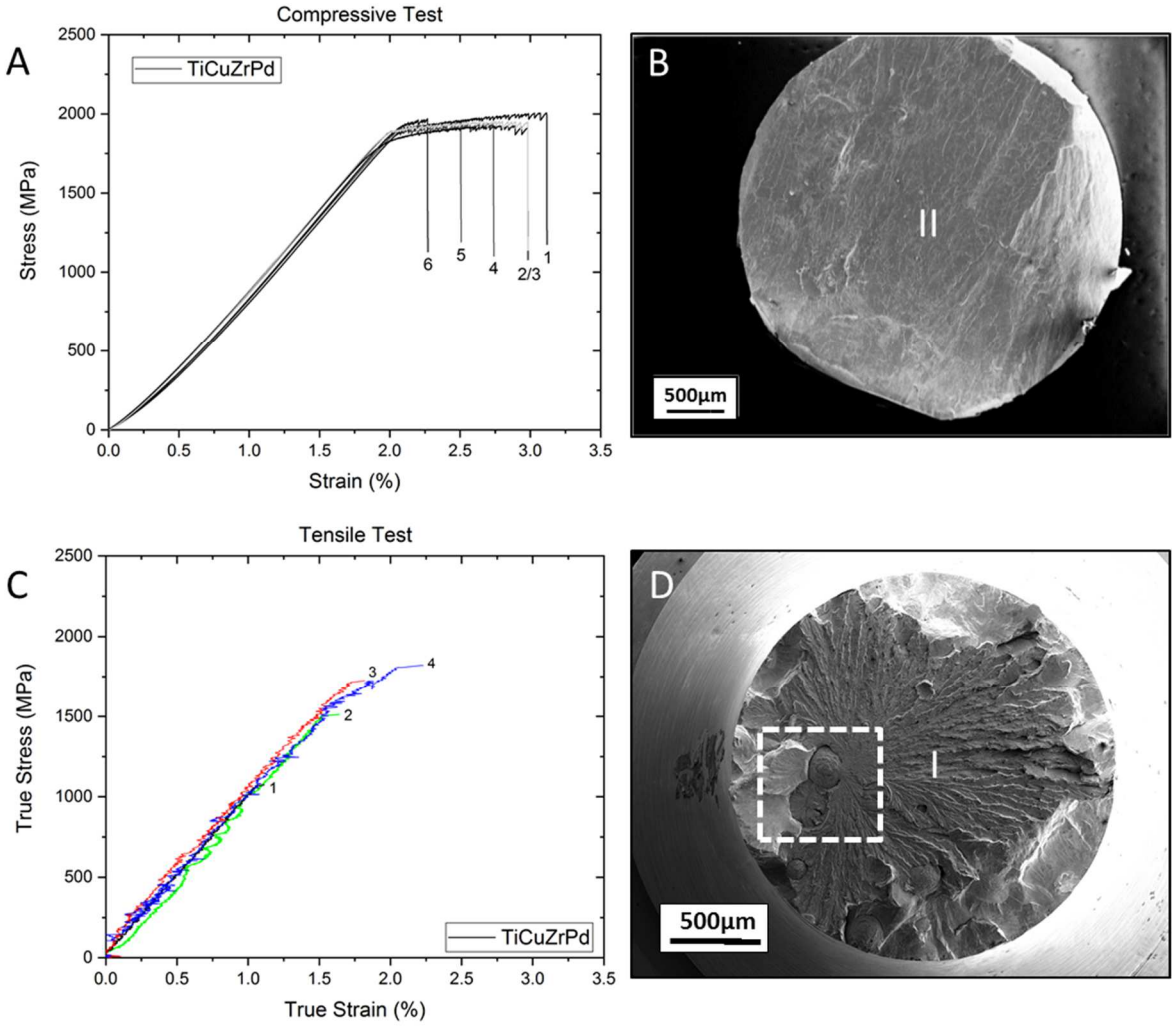

Figure 8: (A) compressive stress-strain curves obtained on 6 samples of TiCuZrPd BMG with (B) SEM picture of a representative fracture surface extract from [2]. (C) tensile true stress-strain curves obtained on 4 samples of TiCuZrPd with (D) SEM picture of a representative fracture surface which illustrates the presence of casting defects.

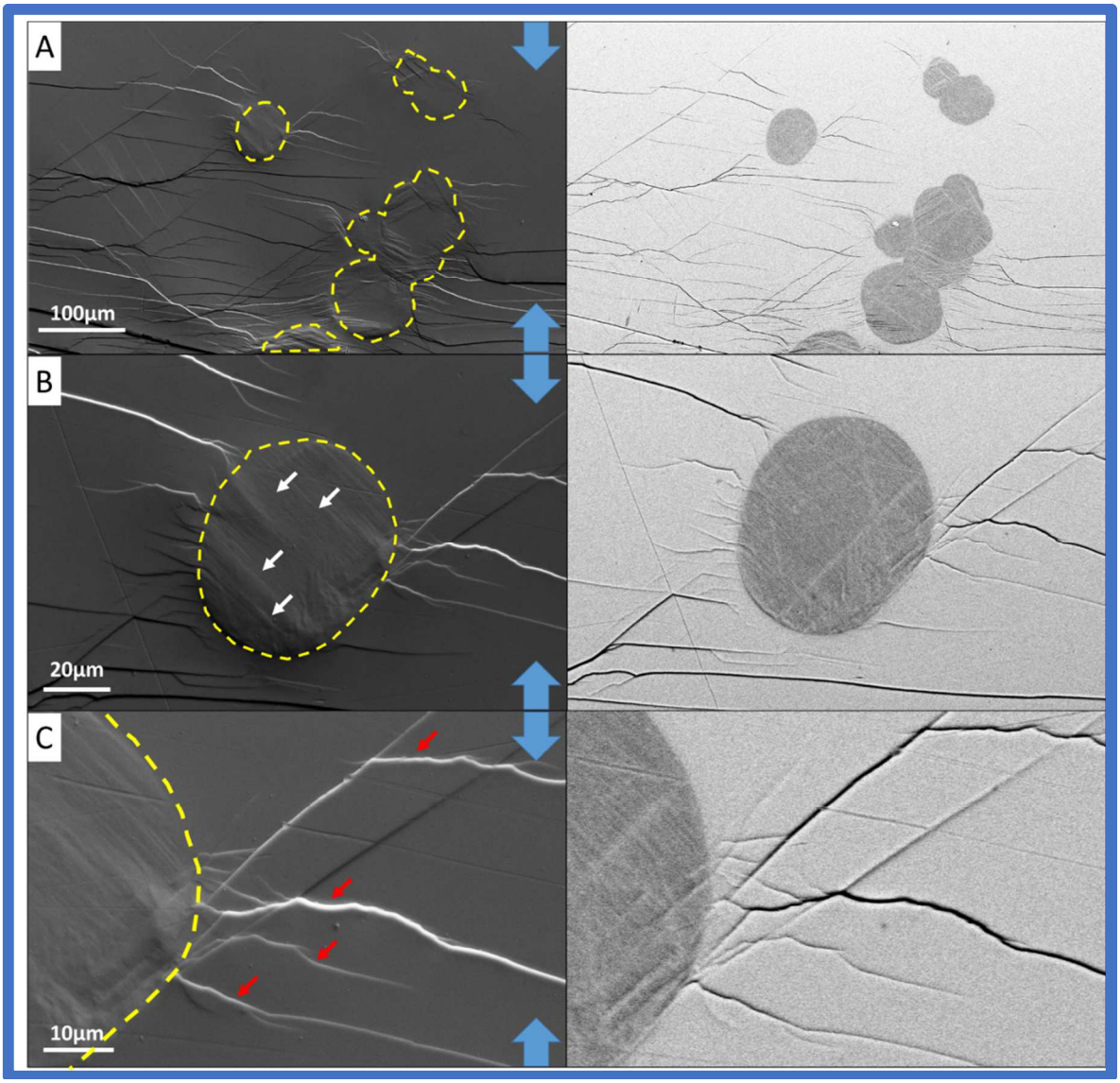

Figure 9: (A) SEM picture at the surface a compression specimen after testing (failure at 1.8GPa) in SE (left) and BSE (right) mode. (B) Higher magnification of one spherulite after the compression. (C) Higher magnification at the interface between the spherulite and the amorphous matrix. The blue arrows symbolize the direction of the compression test. Red arrows represent the shear bands in the amorphous matrix and the white arrows represent the plastic deformation through dislocation movement inside the spherulites.

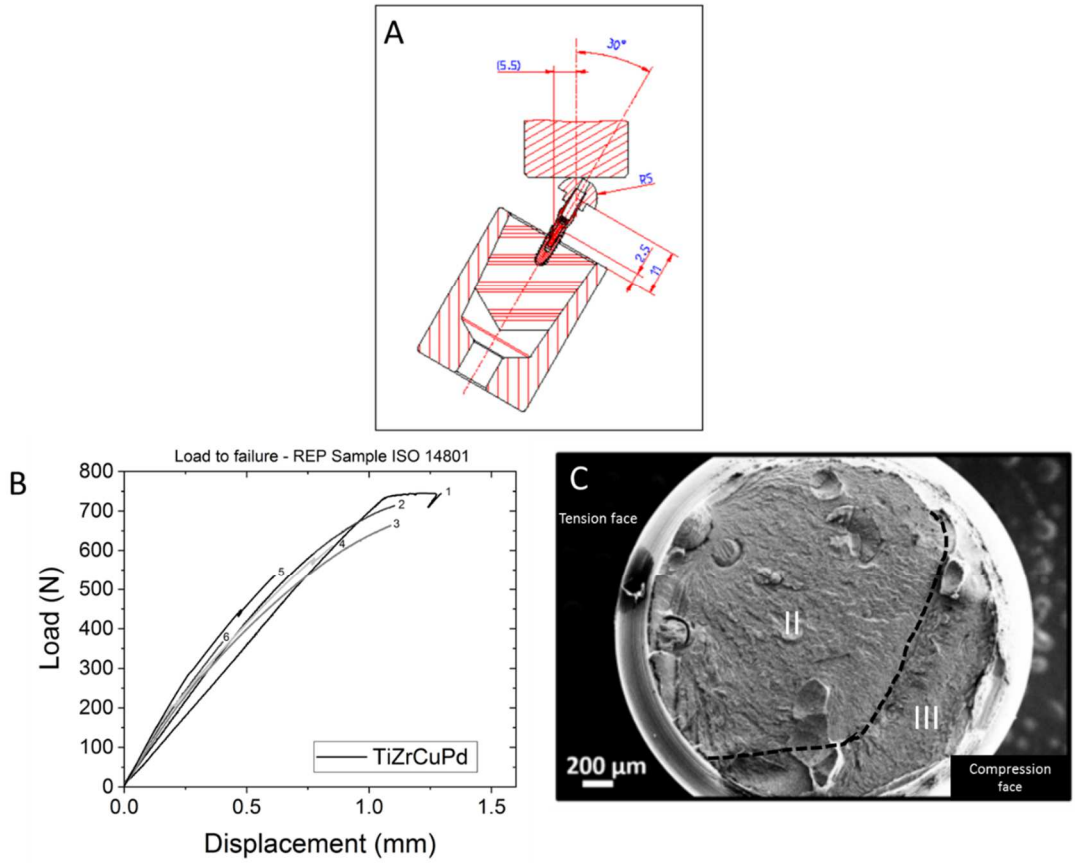

Figure 10: (A) scheme of the ISO 14801 mechanical test on dental implants. (B) load displacement curves on 6 dental implant prototypes (REPSAMPLES). (C) representative fracture surface.

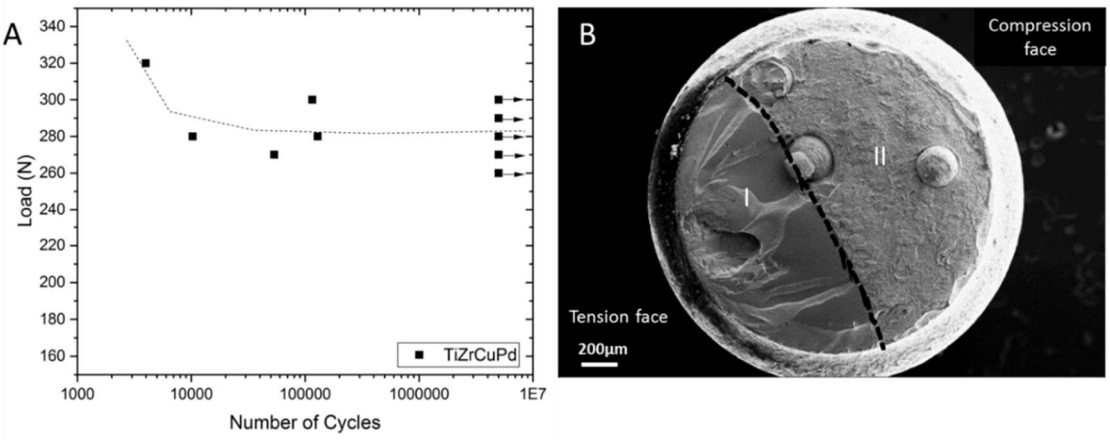

Figure 11 : (A) typical fatigue Wöhler curve (cycles to failure versus maximum applied load) deduced from a staircase method test on 5 dental implant prototypes. (B) Typical SEM picture of a sample fracture surface.

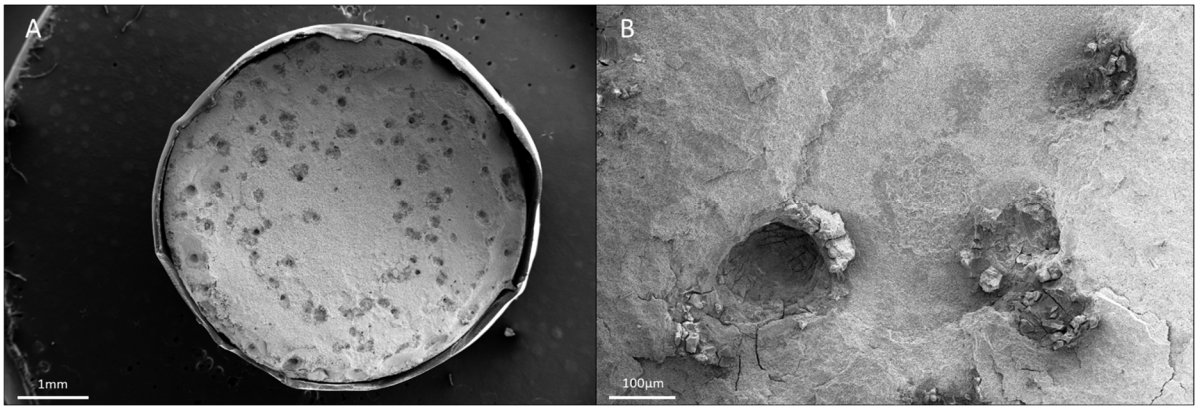

Figure 12: (A) SEM picture of one TiCuZrPd sample after polarization from -0.5 to 1V vs Ag/AgCl in a 0.9% NaCl solution obtained after 6 hours of immersion. (B) higher magnification of the sample's surface state after the test.

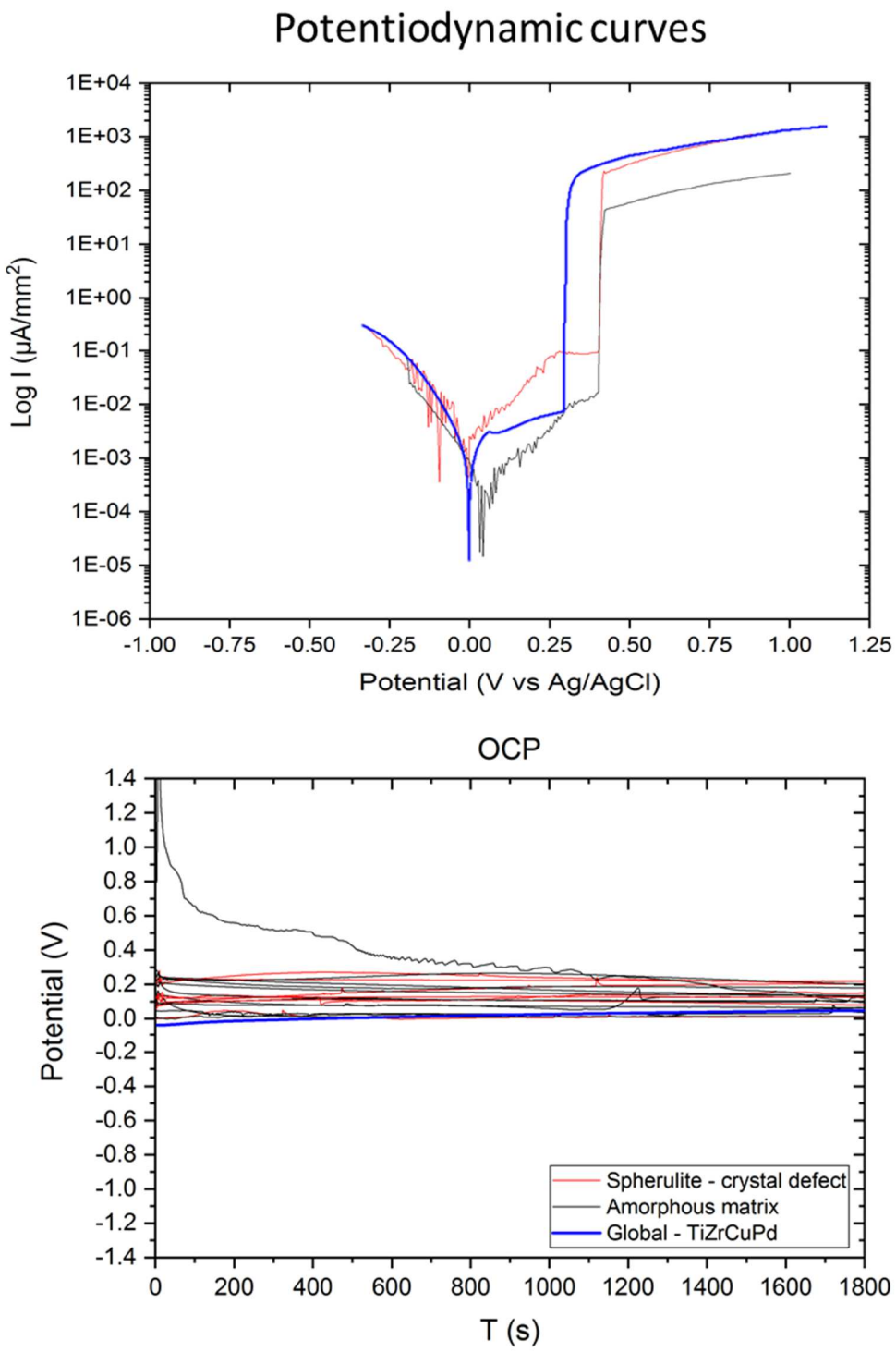

Figure 13: (A) potentiodynamic curves of local measurements on spherulite (red curves) or amorphous matrix (black curves). (B) Open Circuit Potential (OCP) local measurements on spherulite (red curves) or amorphous matrix (black curves). The blue curves are reported for comparison purpose from [17].

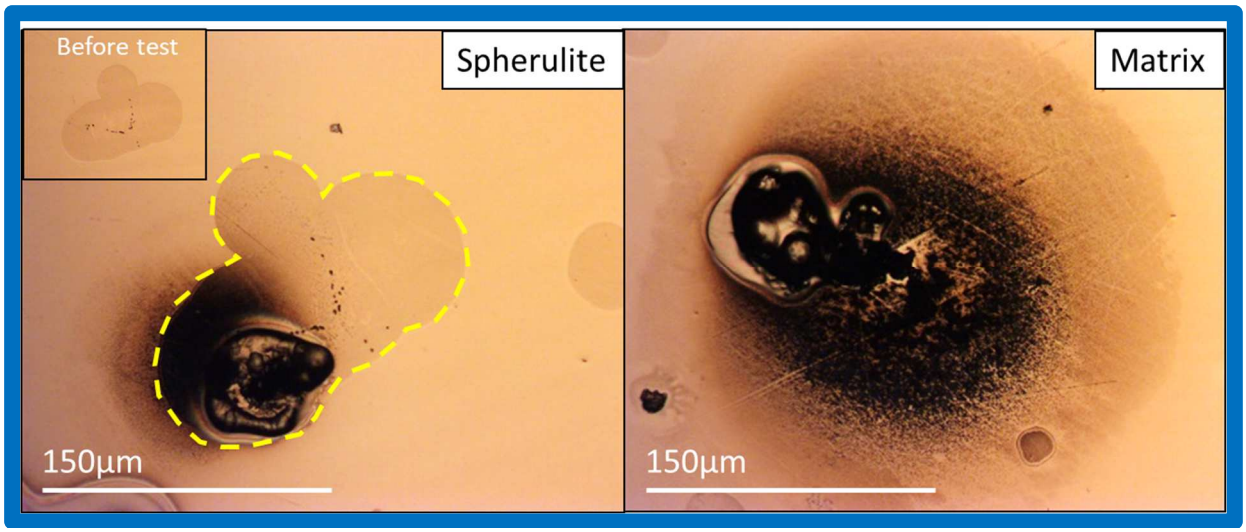

Figure 14: Optical observations of the surface of one sample after local corrosion measurements. Left: Spherulite (the insert shows the spherulite before the local corrosion test). Right: Amorphous matrix.

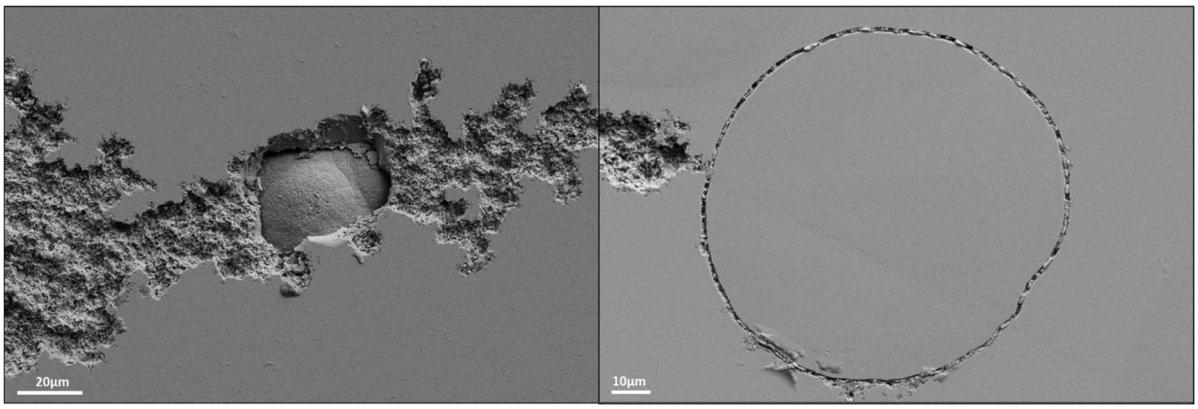

Figure 15: SEM pictures of one TiCuZrPd sample after a cyclic polarization in NaCl 0.9%. The shell at the interface between amorphous matrix and spherulite seems to dissolve preferentially.

Table 1: Hardness Vickers measurements on amorphous matrix and spherulites.

	Hardness (HV)
Spherulites	307 (± 3.5 HV)
Amorphous matrix	556 (± 4.5 HV)

Table 2: Young's modulus (E), compressive strength (σ_{max}), elastic strain (ε_e), plastic strain (ε_p), load to failure and fatigue limit for TiCuZrPd estimated from the compressive, tensile, load to failure and fatigue curves.

Alloy	Test	E (GPa)	σ_{max} (MPa)	ε_e (%)	ε_p (%)	Load to failure (N)	Fatigue limit (N)
TiZrCuPd	Compression	105±1	2010±15	2±00.5	0.3 – 0.7	/	/
	Tension	97.5±1.8	1075 - 1820	1.6±0.3	0.05 – 0.19	/	/
	ISO 14801	/	/	/	/	600±136	300

Table 3 : Summary of the 4-point bending tests on SEVNB samples. a: notch dimension, σ_{max}: maximum stress recorded, K_{IC} : calculated critical stress intensity factor.

Material	Test	a (mm)	σ_{max} (MPa)	KIC ($MPa.\sqrt{m}$)
TiZrCuPd	4 points bending test SEN(V)B	213 - 261	612 - 1005	32 - 42

Graphical abstract